Journal of Fluids and Structures 17 (2003) 225–242

JOURNAL OF
FLUIDS AND
STRUCTURES

www.elsevier.nl/locate/jnlabr/yjfls

Flutter and limit cycle oscillations of two-dimensional panels in three-dimensional axial flow

D.M. Tang[a], H. Yamamoto[b], E. H. Dowell[a,*]

[a] *Department of Mechanical Engineering and Materials Science, Duke University, Durham, NC 27708-0300, USA*
[b] *Department of Mechanical Engineering, Saitama University, Saitama, Japan*

Received 30 May 2001; accepted 8 July 2002

Abstract

Experimental flutter and limit cycle oscillations (LCO) of two-dimensional elastic plates in three-dimensional axial flow were observed. The plate is clamped at its leading edge and free at its trailing edge, i.e., it is a “flag” albeit one dominated by its bending stiffness. In the companion theoretical model the structural nonlinearity arises in both the bending stiffness and the mass inertia. Aerodynamic nonlinearities are neglected, however, and linear three-dimensional incompressible vortex lattice aerodynamic theory and a corresponding reduced order aerodynamic model were used to calculate the linear flutter boundary and also the LCO (that occur beyond the linear flutter boundary). The results from the theory and experiment are in good agreement for the onset of flutter, including the critical flow velocity at which the aeroelastic system becomes unstable, as well as the aeroelastic mode of oscillation and frequency. However, there are significant differences between the present theory and experiment for large-amplitude LCO. It is hypothesized that aerodynamic nonlinearities (not modelled in the present theory) are the primary cause of these differences.

1. Introduction

Flutter and limit cycle oscillations (LCO) of plates with free edges representative of some low aspect ratio wings have been studied experimentally by Doggett and Solstmann (1989). Recently, investigations at low subsonic flow speeds by Tang et al. (1999, 2001a,b) have used Von Karman plate equations and a three-dimensional time domain vortex lattice aerodynamic model and reduced order aerodynamic technique to investigate theoretically the flutter and limit cycle oscillation characteristics of a cantilevered low aspect ratio, rectangular or delta wing-panel structure cantilevered from a side edge parallel to the aerodynamic flow. Flutter and limit cycle oscillations (LCO) were found and correlated well with experiment, see Tang et al. (1999, 2001a,b).

As distinct from the above configurations, a two-dimensional cantilevered panel clamped at its leading edge and free at its trailing edge in a three-dimensional incompressible axial flow is considered in this paper. For this model, earlier studies have been made by Kornecki et al. (1976) and also by Huang (1995) and Shayo (1980) for a similar, but linear structural model in a two-dimensional flow. The results of these investigators were concerned with linear aeroelastic instability, i.e., the onset of flutter. Recent theoretical work by Tang and Dowell (2001a,b) has considered the structural nonlinearities that arise in the bending stiffness and mass inertia of the structure. A two-dimensional time domain (linear) vortex lattice aerodynamic theory and a corresponding reduced order aerodynamic model were used by Tang and Dowell (2001a,b) in conjunction with an appropriate structural model. Both flutter and LCO were determined. Complementing Tang and Dowell (2001a,b), in the present paper the focus of the work is on the experimental

---

*Corresponding author. Tel.: +919-660-5302; fax: +919-660-0089.
E-mail address: dowell@ee.duke.edu (E. H. Dowell).

0889-9746/03/$ - see front matter © 2002 Elsevier Science Ltd. All rights reserved.
PII: S0889-9746(02)00121-4

Nomenclature

b	width of elastic panel
c	total length of airfoil and panel in the chordwise direction, $c = L_0 + L$
D	panel bending stiffness, $Eh^3/[12(1-\nu^2)]$
E	modulus of elasticity
h	panel thickness
L	length of elastic panel
L_0	length of rigid airfoil in chordwise direction
$k_m,\ k_n$	numbers of vortex elements on the rigid airfoil and elastic panel, respectively
k_{mm}	total number of vortices on the rigid airfoil, the panel and the wake in the x-direction
m_p	mass/area of elastic panel, $m_p = h\rho_m$
nx	number of structural modal functions defining w
q_i	structural generalized coordinate in the z-direction
Q_i	generalized aerodynamic force
R_a	size of the reduced order aerodynamic model
t	time
u	in-plane deflection in the x-direction
U	airspeed
U_f	linear flutter airspeed
w	elastic panel deflection in the transverse or z-direction
$x,\ z$	streamwise and normal coordinates
$[X],\ [Y]$	right and left eigenvector matrices of vortex lattice aerodynamic eigenvalue model
$[Z]$	eigenvalue matrix of vortex lattice model
τ	time parameter, $\tau = \sqrt{m_pL^4/D}$
Δp	aerodynamic pressure loading on panel
$\Delta\bar{p}$	nondimensional aerodynamic pressure, $\Delta p/(\rho_\infty U^2)$
$\mathrm{d}t$	the time step, $\mathrm{d}x/U$
$\mathrm{d}x$	panel element length in the streamwise direction
Γ	the vortex strength
$\rho_\infty,\ \rho_m$	air and panel material densities
ν	Poisson's ratio
$\omega_f,\ \omega$	flutter frequency and oscillation frequency
ω_m	natural frequency
$(\dot{\ })$	$\mathrm{d}(\,)/\mathrm{d}t$
$(\,)'$	$\mathrm{d}(\,)/\mathrm{d}x$

validation of the predicted flutter and LCO. To that end, a two-dimensional cantilevered panel in a three-dimensional axial flow was designed and tested. A photoelectric technique was used to measure the LCO response. Appropriate to the experimental model, the theoretical analysis used a three-dimensional time domain vortex lattice aerodynamic model. However, the structural response per se is essentially one-dimensional in the axial flow direction, i.e., no significant bending of the panel occurs in the spanwise direction.

We also note the interesting work of Taneda (1968) and Yadykin et al. (2000) both of whom considered two-dimensional "flags" in a three-dimensional flow. Taneda's work is experimental and he used flags made of "silk, muslin, flannel, blanked and canvas". Yadykin et al. did experiments as well as constructed a nonlinear structural theory in combination with a linear "slender body" aerodynamic model appropriate to very low aspect ratios in combination with an empirical aerodynamic correction for drag. Yadykin's theoretical/experimental correlations are for drag, rather than for the flutter onset condition and structural limit cycle oscillation response which is the focus of the present paper.

Among the contributions of this paper are the following. It is the first to use a true three-dimensional aerodynamic theory based upon potential flow (as contrasted with a two-dimensional aerodynamic theory which is appropriate for very high aspect ratios or slender body theory which is an approximation for very low aspect ratios), the first to achieve good correlation for the onset of flutter between theory and experiment for a two-dimensional plate cantilevered at its leading edge in a three-dimensional flow, and the first to attempt (not altogether successfully to be sure) correlation between theory and experiment for LCO for the same flow conditions and structural configuration.

2. State-space equations

A schematic of the airfoil/panel geometry with a three-dimensional vortex lattice model of the unsteady flow is shown in Fig. 1. The aeroelastic structure/fluid state-space equations are described as follows.

2.1. Aerodynamic model

To model the above aeroelastic structural/fluid system, we consider a flat elastic panel with finite width, b and length, L. It is clamped at its leading edge to a rigid airfoil that spans the wind tunnel and has a finite length, L_0. The total length or chord of the rigid airfoil plus elastic panel system is $L + L_0$. The flow about the rigid airfoil/cantilevered panel is assumed to be incompressible, inviscid and irrotational. Here we use an unsteady (linear) three-dimensional vortex lattice method to model this flow, see Tang et al. (1999, 2001a,b). The rigid airfoil/cantilevered panel and wake are divided into a number of flow elements. In the wake and on the rigid airfoil/cantilevered panel all the flow elements are of equal size, dx, in the streamwise direction. Point vortices are placed on the rigid airfoil/cantilever panel and in the wake at the quarter chord of the elements. At the three quarter chord of each panel element a collocation point is placed for the downwash, i.e., we require the velocity induced by the discrete vortices to equal the downwash arising from the unsteady motion of the cantilever panel. Thus, we have the relationship,

$$w_i^{t+1} = \sum_{j}^{k_{mm}} K_{ij}\Gamma_j^{t+1}, \quad i = 1, \ldots, k_m, \tag{1}$$

where w_i^{t+1} is the downwash at the ith collocation point at time step $t+1$, Γ_j is the strength of the jth vortex, and K_{ij} is an aerodynamic kernel function for the horseshoe vortex. For the three-dimensional incompressible flow, the kernel function is given by Joseph and Allen (1991)

$$K_{ij} = \frac{-1}{4\pi(y_i - y_{ja})}\left[1 + \frac{\sqrt{(x_i - x_{ja})^2 + (y_i - y_{ja})^2}}{x_i - x_{ja}}\right] + \frac{1}{4\pi(y_i - y_{jb})}\left[1 + \frac{\sqrt{(x_i - x_{ja})^2 + (y_i - y_{jb})^2}}{x_i - x_{ja}}\right], \tag{2}$$

where x_i is the location of the ith collocation point, and y_{ja} and y_{jb} are the location of the two jth trailing vortex segments which are parallel to the x-axis at $y = y_a$ and y_b.

The aerodynamic matrix equation is given by

$$[A]\{\Gamma\}^{t+1} + [B]\{\Gamma\}^{t} = \{w\}^{t+1}, \tag{3}$$

where $[A]$ and $[B]$ are aerodynamic coefficient matrices.

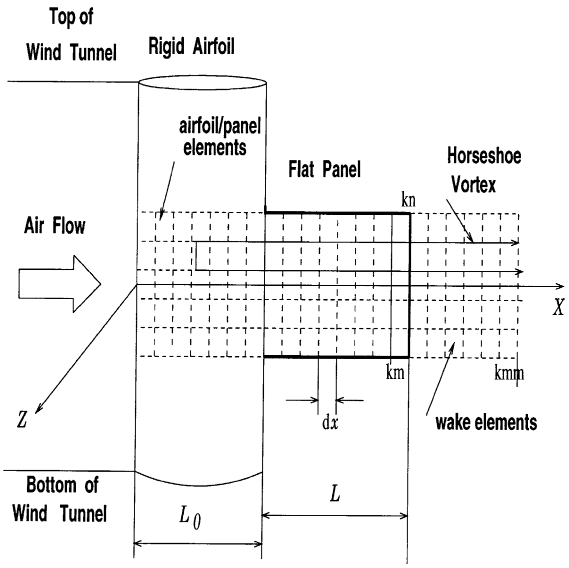

Fig. 1. Schematic of the airfoil/panel geometry with a three-dimensional vortex lattice model of the unsteady flow.

The nondimensional pressure distribution on the rigid airfoil/flat panel is given by

$$\overline{\Delta p_j} = \frac{c}{\mathrm{d}x}[(\Gamma_j^{t+1} + \Gamma_j^t)/2 + \sum_i^j (\Gamma_i^{t+1} - \Gamma_i^t)] \tag{4}$$

and the aerodynamic generalized force is calculated from

$$Q_i = \rho_\infty U^2 \int_0^c \overline{\Delta p} \Phi_i \, \mathrm{d}x, \tag{5}$$

where Φ_i is ith downwash mode function

$$\Phi_i = \begin{cases} 0 & \text{for } x \leqslant L_0, \\ \phi_i & \text{for } L + L_0 \geqslant x > L_0 \end{cases}$$

and ϕ_i is ith structural mode function of a two-dimensional cantilevered flat elastic panel.

2.2. Structural equations of motion

We now proceed to calculate the kinetic and potential energy of the two-dimensional cantilevered flat elastic panel. (Note that the energies of the rigid airfoil are neglected.) Thus, the equations of motion may be derived via Hamilton's principle.

For the present structural model, an axially inextensible assumption is used here for the in-plane motion of the elastic panel. Following the analysis of Semler and Paidoussis (1994), the inextensibility condition may be expressed as

$$\left(1 + \frac{\partial u}{\partial x}\right)^2 + \left(\frac{\partial w}{\partial x}\right)^2 = 1. \tag{6}$$

We use the classical expressions for kinetic and potential energy of an elastic body, but include nonlinear stiffness and inertia effects. Thus the expressions for the energies are as follows. For a more in-depth discussion of the structural model, see the book by Paidoussis (1998).

2.2.1. Kinetic energy

The kinetic energy is given by

$$T = \frac{1}{2} \int_0^L m_p (\dot{u}^2 + \dot{w}^2) \, \mathrm{d}x, \tag{7}$$

If the panel transverse deflection in the z-direction (w) is considered to be small relative to the panel length, then the term, $(\partial u/\partial x)^2$, in Eq. (6) may be neglected compared to $\partial u/\partial x$.

Thus, for $u = 0$ at $x = 0$ and from Eq. (6) we have

$$u(x) = -\frac{1}{2} \int_0^x \left(\frac{\partial w}{\partial x}\right)^2 \mathrm{d}x, \tag{8}$$

2.2.2. Potential energy

The potential energy is

$$V = \frac{1}{2} \int_0^L D(\psi'')^2 \, \mathrm{d}x, \tag{9}$$

where ψ'' is nonlinear curvature of the two-dimensional panel, see Semler and Paidoussis (1994),

$$\psi'' = \frac{\partial^2 w}{\partial x^2} \Bigg/ \left[1 - \left(\frac{\partial w}{\partial x}\right)^2\right]^{1/2}$$

and $D \equiv Eh^3/[12(1 - \nu^2)]$. Thus for $(\partial w/\partial x)^2 \ll 1$,

$$(\psi'')^2 \approx \left(\frac{\partial^2 w}{\partial x^2}\right)^2 \left[1 + \left(\frac{\partial w}{\partial x}\right)^2\right]. \tag{10}$$

Substituting Eq. (10) into Eq. (9) gives

$$V = \frac{1}{2}\int_0^L D\left(\frac{\partial^2 w}{\partial x^2}\right)^2\left[1+\left(\frac{\partial w}{\partial x}\right)^2\right]\mathrm{d}x. \tag{11}$$

2.2.3. Hamilton's principle

The energy method is based on Hamilton's principle which may be written as

$$\delta\int_{t_1}^{t_2}\mathrm{La}\,\mathrm{d}t + \int_{t_1}^{t_2}\delta W\,\mathrm{d}t = 0, \tag{12}$$

where La is the Lagrangian of the system ($\mathrm{La} = T - V$) and δW is the virtual work due to aerodynamic force.

The variational operations on La lead to

$$\delta\int_{t_1}^{t_2}\mathrm{La}\,\mathrm{d}t = m_p\int_{t_1}^{t_2}\int_0^L(\dot{u}\,\delta u + \dot{w}\,\delta w)\,\mathrm{d}t\,\mathrm{d}x + \frac{D}{2}\int_{t_1}^{t_2}\int_0^L\delta\left[\left(\frac{\partial^2 w}{\partial x^2}\right)^2\left(1+\left(\frac{\partial w}{\partial x}\right)^2\right)\right]\mathrm{d}t\,\mathrm{d}x. \tag{13}$$

Integrating by parts, one obtains

$$\delta\int_{t_1}^{t_2}T\,\mathrm{d}t = -m_p\int_{t_1}^{t_2}\int_0^L[\ddot{u}\,\delta u + \ddot{w}\,\delta w]\,\mathrm{d}t\,\mathrm{d}x, \tag{14}$$

where

$$\ddot{u} = -\frac{1}{2}\int_0^x\left(\frac{\partial\ddot{w}}{\partial x}\right)^2\mathrm{d}x,$$

$$\delta\int_{t_1}^{t_2}V\,\mathrm{d}t = D\int_{t_1}^{t_2}\int_0^L\left[\frac{\partial^4 w}{\partial x^4} + 4\frac{\partial w}{\partial x}\frac{\partial^2 w}{\partial x^2}\frac{\partial^3 w}{\partial x^3} + \left(\frac{\partial^2 w}{\partial x^2}\right)^3 + \frac{\partial^4 w}{\partial x^4}\left(\frac{\partial w}{\partial x}\right)^2\right]\delta w\,\mathrm{d}t\,\mathrm{d}x \tag{15}$$

and

$$\int_{t_1}^{t_2}\delta W\,\mathrm{d}t = \int_{t_1}^{t_2}\int_0^L\Delta p\,\delta w\,\mathrm{d}x\,\mathrm{d}t. \tag{16}$$

A relationship between the virtual displacements δu and δw may be obtained using the inextensibility condition. It is

$$\delta\frac{\partial u}{\partial x} = -\frac{\partial w}{\partial x}\left[1+\frac{1}{2}\left(\frac{\partial w}{\partial x}\right)^2\right]\delta\frac{\partial w}{\partial x}. \tag{17}$$

Integrating Eq. (17) and applying the boundary conditions, $\delta w = 0$ at $x = 0$, one obtains

$$\delta u = -\left(\frac{\partial w}{\partial x} + \frac{1}{2}\left(\frac{\partial w}{\partial x}\right)^3\right)\delta w + \int_0^x\left(\frac{\partial^2 w}{\partial x^2} + \frac{3}{2}\left(\frac{\partial w}{\partial x}\right)^2\frac{\partial^2 w}{\partial x^2}\right)\delta w\,\mathrm{d}x. \tag{18}$$

Substituting Eq. (18) into Eq. (14) and using Eqs. (12), (15) and (16) and the following integration formula:

$$\int_0^L g(x)\int_0^x f(x)\,\delta w\,\mathrm{d}x\,\mathrm{d}x = \int_0^L\left(\int_x^L g(x)\,\mathrm{d}x\right)f(x)\,\delta w\,\mathrm{d}x,$$

one obtains the final structural equation of motion as

$$m_p\ddot{w} + D\left[\frac{\partial^4 w}{\partial x^4}\left(1+\left(\frac{\partial w}{\partial x}\right)^2\right) + 4\frac{\partial w}{\partial x}\frac{\partial^2 w}{\partial x^2}\frac{\partial^3 w}{\partial x^3} + \left(\frac{\partial^2 w}{\partial x^2}\right)^3\right] - \frac{\partial^2 w}{\partial x^2}\int_s^L\int_0^x m_p\left(\left(\frac{\partial\dot{w}}{\partial x}\right)^2 + \frac{\partial w}{\partial x}\frac{\partial\ddot{w}}{\partial x}\right)\mathrm{d}x\,\mathrm{d}x$$
$$+\frac{\partial w}{\partial x}\int_0^x m_p\left(\left(\frac{\partial\dot{w}}{\partial x}\right)^2 + \frac{\partial w}{\partial x}\frac{\partial\ddot{w}}{\partial x}\right)\mathrm{d}x = \Delta p. \tag{19}$$

We now expand the transverse or out-of-plane displacement, w, as follows:

$$w = \sum_m q_m(t)\phi_m(x), \tag{20}$$

where the transverse natural mode function, $\phi_m(x)$ is that of a cantilevered beam. These functions satisfy the boundary conditions of the cantilevered panel.

Substituting Eq. (20) into Eq. (19), multiplying by $\phi_i(x)$ and integrating from 0 to 1, gives the (nonlinear) equations of motion:

$$M_{ii}\ddot{q}_i + \sum_n \sum_r \sum_s M_{inrs} q_n q_r \ddot{q}_s + \omega_i^2 M_{ii} q_i + F_K + F_M = Q_i, \tag{21}$$

where q_i is normalized by L. The nonlinear force F_K is induced by the nonlinear curvature of the restrained panel while F_M plus $\sum_n \sum_r \sum_s M_{inrs} q_n q_r \ddot{s}$ are the nonlinear inertia terms. They are, respectively,

$$F_K = \sum_n \sum_r \sum_s K_{inrs} q_n q_r q_s$$

and

$$F_M = \sum_n \sum_r \sum_s M_{inrs} q_n \dot{q}_r \dot{q}_s,$$

where

$$M_{ii} \equiv \int_0^1 m_p \phi_i^2 \, \mathrm{d}x,$$

$$K_{inrs} = \int_0^1 D\phi_i \left[\phi_n'''' \phi_r' \phi_s' + 4\phi_n' \phi_r'' \phi_s''' + \phi_n'' \phi_r'' \phi_s''\right] \mathrm{d}x,$$

$$M_{inrs} = \int_0^1 m_p \phi_i \phi_n' \left(\int_0^x \phi_r' \phi_s' \, \mathrm{d}x \right) \mathrm{d}x - \int_0^1 m_p \phi_i \phi_n'' \left(\int_x^1 \int_0^x \phi_r' + \phi_s' \, \mathrm{d}x \, \mathrm{d}x \right) \mathrm{d}x.$$

2.3. *Aeroelastic state-space equations*

Consider a discrete time history of the panel, $q(t)$, with a constant sampling time step, Δt. The structural dynamic equations, Eq. (21), can be reconstituted as a state-space equation in discrete time form, i.e.,

$$\left[D_2 + \mathrm{d}M(q_n^t, q_s^t)\right]\{\theta\}^{t+1} + [D_1]\{\theta\}^t + [C_2]\{\Gamma\}^{t+1} + [C_1]\{\Gamma\}^t = -\{F_N\}^{t+1/2}, \tag{22}$$

where the vector $\{\theta\}$ is the state of the panel, $\{\theta\} = \{\dot{q}, q\}$ and $[D_1], [D_2]$ are matrices describing the panel structural behavior. $[\mathrm{d}M(q_n^t, q_s^t)]$ is an additional nonlinear mass matrix which depends on the structural response itself. $[C_1], [C_2]$ are matrices describing the vortex element forces on the airfoil/panel. The nondimensional nonlinear force F_N is given by

$$F_N = F_K/\tau^2 + F_M/(m_p L^2).$$

There is a linear relationship between the downwash w at the collocation points and panel response, $\{\theta\}$. It is defined by

$$\{w\} = [E]\{\theta\}. \tag{23}$$

Thus, combining Eqs. (3), (22) and (23), we obtain a complete aeroelastic state-space equation in matrix form.

$$\begin{bmatrix} A & -E \\ C_2 & D_2 + \mathrm{d}M(q_n^t, q_s^t) \end{bmatrix} \begin{Bmatrix} \Gamma \\ \theta \end{Bmatrix}^{t+1} + \begin{bmatrix} B & 0 \\ C_1 & D_1 \end{bmatrix} \begin{Bmatrix} \Gamma \\ \theta \end{Bmatrix}^{t} = \begin{Bmatrix} 0 \\ -F_N \end{Bmatrix}^{t+1/2}. \tag{24}$$

Following a similar treatment as described by Tang et al. (1999, 2001), a reduced order aerodynamic model with static correction is constructed and the final aeroelastic state-space model is given by

$$\begin{bmatrix} I & -Y_{Ra}^{\mathrm{T}}[I - A(A+B)^{-1}]E \\ C_2 X_{Ra} & D_2 + \mathrm{d}M(q_n^t, q_s^t) + (C_2(A+B)^{-1}E \end{bmatrix} \begin{Bmatrix} \gamma_d \\ \theta \end{Bmatrix}^{t+1} + \begin{bmatrix} -Z_{Ra} & Y_{Ra}^{\mathrm{T}} B(A+B)^{-1}E \\ C_1 X_{Ra} & D_1 + C_1(A+B)^{-1}E \end{bmatrix} \begin{Bmatrix} \gamma_d \\ \theta \end{Bmatrix}^{t} = \begin{Bmatrix} 0 \\ -F_N \end{Bmatrix}^{t+1/2}, \tag{25}$$

where γ is the vector of the aerodynamic modal coordinates and $\Gamma = X_{Ra}\gamma$.

3. Experimental model and measurement procedures

Fig. 2 shows the physical representation of the wing/panel model. The two-dimensional wing model includes two parts: a flexible rectangular aluminum panel of thickness 0.0155 in (0.39 mm), width 5 in (127 mm) and length 10.5 in (266.7 mm) that is exposed to the aerodynamic flow and an additional length of 3 in (76.2 mm) that is internal to the clamped rigid airfoil support.

The rigid airfoil support was made of solid aluminum with a NACA 0015 section. The chord is 4 in (101.6 mm) and the span is 22 in (559 mm) with both ends clamped at the top and bottom (center-line) of a wind tunnel. The flat elastic plate is located at the mid-span and trailing edge of the rigid airfoil. The clamped surface of the flexible panel is placed on the flat rigid airfoil support and bonded using M-bond 200 adhesive. Another (relatively stiff) flat plate of 3×5 in (76.2×127 mm) is bonded to the flexible panel and is also fixed to the rigid airfoil support using 10 screws. The purpose of this construction is to satisfy the clamped boundary condition at the trailing edge of the rigid support airfoil and leading edge of the flexible plate. The rigid airfoil section in the clamping area is also machined to be a NACA 0015 airfoil.

Axial strain gages were glued to the root of the flexible panel to measure bending deflections. Signals from the strain gages were conditioned and amplified before recording through a gage conditioner and a low-pass filter. The output signals from these transducers are directly recorded and analyzed on a FFT analyzer.

A digital camera and a strobotac are also mounted on the top of the wind tunnel to measure the panel responses. The calibration procedure is as follows. Before taking pictures of the responses of panel from the top of the wind tunnel, a plate is placed on the top edge of the elastic panel to take a reference picture of it. A grid is drawn on the plate and this grid separates the plane into 0.1 in (2.54 mm) squares in the x- and y-directions. Finally, the dynamic responses of the elastic panel are measured and then we superimpose the reference picture of the plate and that of the response using a PC to measure the amplitude of the top edge of the elastic panel.

The mean wind tunnel flow velocity is measured by a conventional Pitot tube.

4. Results from theory and experiment

For the present computational and experimental model, we consider an aluminum panel (7075 material), $\rho_m = 2.84 \times 10^3\ \mathrm{kg/m^3}$, $E = 7.2 \times 10^9\ \mathrm{kg/m^2}$, $\nu = 0.3$, $L = 0.27\ \mathrm{m}$, $L_0 = 0.1\ \mathrm{m}$. The structural critical damping ratio is taken as 0.005 as determined from a standard measurement. The first three structural bending modes were included in the analysis and the natural frequencies were both computed and measured to be 4.57, 28.62, 80.15 and 4.5, 29.2, 81.2 Hz, respectively. The two results are in good agreement. For the aerodynamic parameters, the airfoil/panel was modelled using 300 vortex elements, i.e., $k_m = 60$, $k_n = 5$. The wake was modelled using 300 vortex elements, i.e., $k_{mm} = 120$. The total number of vortex elements (or aerodynamic degrees of freedom) was thus 600. The vortex relaxation factor was taken to be $\alpha = 0.992$. A convergence study was done to determine the number of structural modes and vortex elements needed in the analysis.

For better understanding of the correlation between theory and experiment, some numerical studies on the forced structural nonlinear response and also the linear flutter boundary were done first.

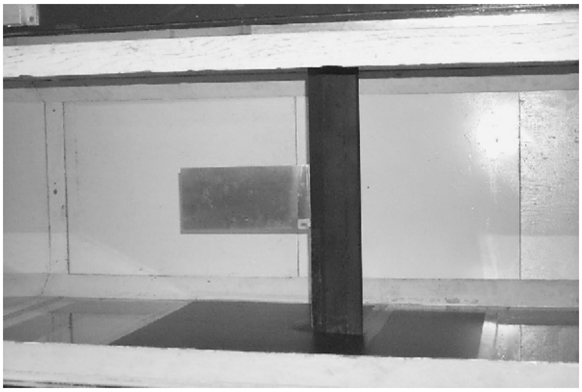

Fig. 2. Photograph of the experimental model in the wind tunnel.

4.1. Preliminary theoretical/numerical analysis

4.1.1. Nonlinear response due to forced excitation

In this case, the aerodynamic force is removed. A single harmonic force $f_0\phi_i(1)\cos(\omega t)$ is placed at the trailing edge of the panel with constant force amplitude ($f_0 = 0.05$. One hundred (100) excitation frequencies ω from 25 to 35 Hz (near the second natural frequency) with $\Delta\omega = 0.1$ Hz are considered. At each frequency, the transient time history is computed until the system achieves a steady-state response. In general, it takes about 20 s (a time step of $dt = 1/2048$ s is used). The time history for the last one second is used to calculate the response amplitude. For the next frequency (increasing $\Delta\omega$), we use initial conditions that are provided by the previous state. This process is continuous in time until the frequency increases to $\omega = 35\,Hz$.

The nondimensional trailing edge response amplitude (w/L) versus excitation frequency (ω) is shown in Fig. 3(a) (in the neighborhood of the second natural frequency) as indicated by the solid line. The peak frequency is 27.9 Hz. This is smaller than the second natural frequency. A jump response is found near $\omega = 27.9$ Hz. In order to consider the mass and stiffness effects of the structural nonlinearity on the response, several different cases were considered as shown in the figures. The broken line shows the linear results, i.e., all nonlinear effects are omitted. These have the largest amplitudes and the corresponding peak frequency is equal to the second natural frequency. The dashed line shows the results with the stiffness nonlinearity only ($dM = F_M = 0$). The peak frequency is 29.3 Hz. This is higher than that for the linear system. A jump response is found near $\omega = 29.3$ Hz, but the response is less than for the linear case. The dash-dot line shows the results for mass inertia nonlinearity only ($F_K = 0$). The peak frequency is 27.6 Hz. Also a jump is found near $\omega = 27.6$ Hz and there is a net smaller amplitude in this frequency range. As shown in Fig. 3(a), the effects of the mass and stiffness nonlinearities are significant in the frequency range near the second natural frequency.

A typical 'time history' of the steady-state response for the last one second at each excitation frequency is shown in Fig. 3(b). The time axis (from 0 to 60 s) in the figure corresponds to the frequency ranging from 26 to 32 Hz. A very clear jump in amplitude at $\omega = 27.9$ Hz was found.

4.1.2. Flutter boundary of the linear aeroelastic model

When the structural nonlinear forces F_N and dM in Eq. (24), or Eq. (25), are set to zero, a linear aeroelastic model is obtained. The aeroelastic eigenvalues obtained from solving these equations determine the stability of the system. When the real part of any one eigenvalue becomes positive, the entire system becomes unstable.

Fig. 4(a,b) show a typical graphical representation of the eigenanalysis in the form of the real part of the eigenvalues (damping) versus the flow velocity and also a root-locus plot for the nominal linear system using all aerodynamic eigenmodes and a reduced order aerodynamic model for the airfoil/panel system. A negative value of the real part of the eigenvalue corresponds to positive damping.

There is an intersection of damping with the velocity axis at $U_f = 29.5$ m/s, the critical flutter velocity using all the aerodynamic modes ($R_a = 600$), with a corresponding flutter oscillatory frequency, $\omega_f = 22.5$ Hz, as indicated by the symbol •. Using a reduced order aerodynamic model with a static correction and only 11 aerodynamic eigenmodes ($R_a = 11$), i.e., the first 11 eigenmodes in the first branch of aerodynamic eigenvalues, the corresponding values are

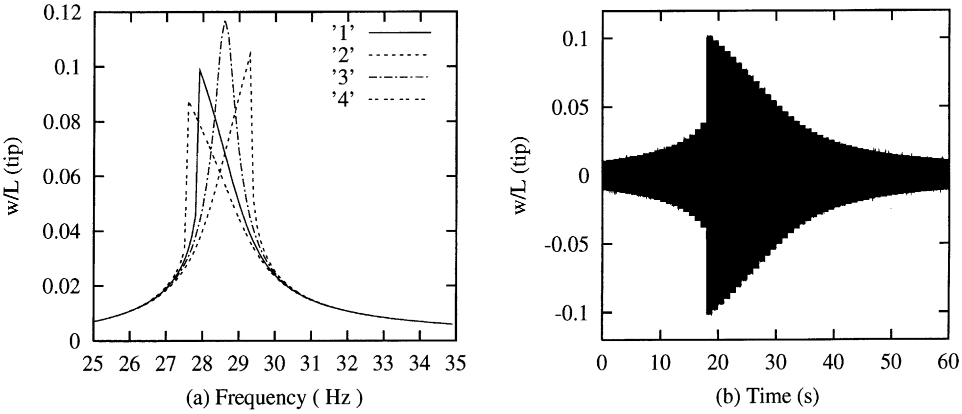

(a) Frequency (Hz) (b) Time (s)

Fig. 3. (a) Frequency response at the trailing edge; "1" is for both stiffness and inertia nonlinearities included, '2' for only stiffness nonlinearity included, '3' for the purely and linear system, '4' for only inertia nonlinearity included; (b) "time history" while increasing the frequency from 26 to 32 Hz.

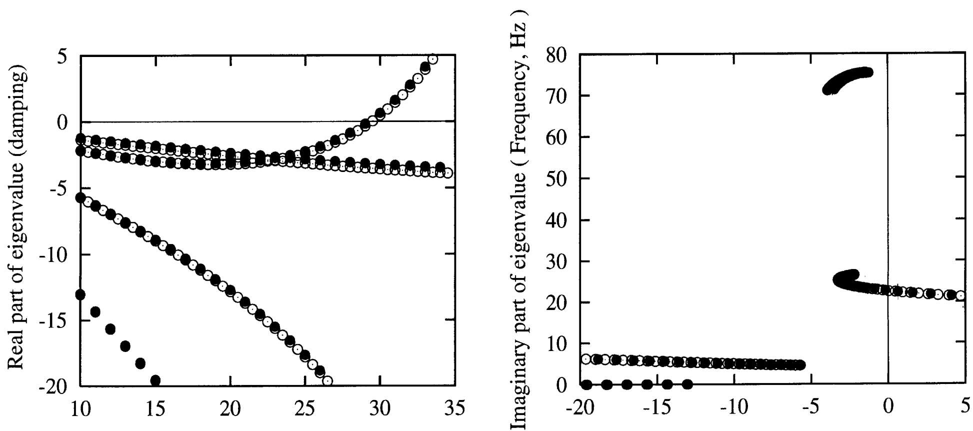

(a) Flow velocity (m/s) (b) Real part of eigenvalue (damping)

Fig. 4. Eigenvalue solution of the linear aeroelastic system (a) for the real part of the eigenvalues and (b) for the root-locus. •, Reduced order aerodynamic model; ◦, all aerodynamic modes included.

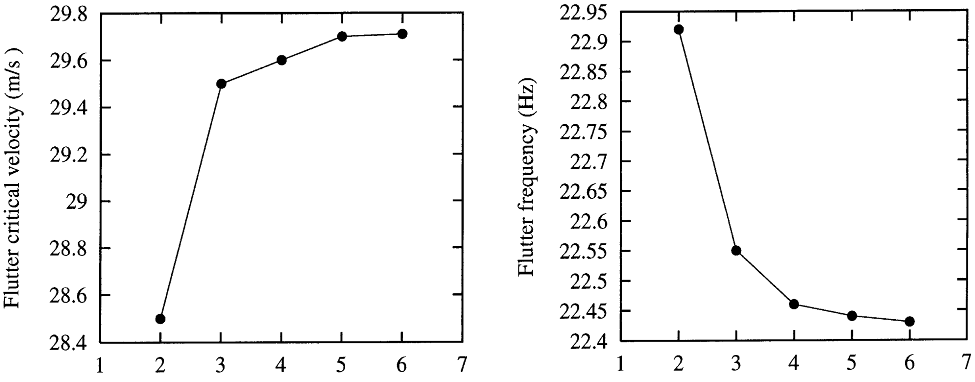

(a) Maximum number of structural modes (b) Maximum number of structural modes

Fig. 5. Eigenvalue solution of the linear aeroelastic system versus number of structural mode, (a) for flutter velocity and (b) for flutter frequency.

indicated by the symbol ◦. The flutter velocity and frequency using the reduced order aerodynamic model are virtually identical to those from the aerodynamic model using all eigenmodes.

To consider effects of the number of structural modal functions, nx, on the flutter critical velocity and frequency, additional aeroelastic eigenvalue calculations for $nx = 2,\ 4,\ 5$ and 6 were made. The results are shown in Fig. 5(a) and (b) for the flutter velocity and frequency versus the number of modes. When $nx \geqslant 3$, the flutter velocity increases slightly as nx increases and good convergence is obtained. For the present model, $nx = 3$ is sufficient.

4.2. Experimental and theoretical results for LCO

4.2.1. Experimental results for LCO

Figs. 6–8 show the responses of the elastic panel for $U = 29.1$, 29.8 and 29.9 m/s, respectively. In this case, the amplitude increases when U increases. However, the amplitude is not so large. So these limit cycle oscillations are called "small-amplitude LCO."

When the rotation speed of the drive motor of the wind tunnel is increased further and the wind tunnel velocity is correspondingly increased to 30.0 m/s, the LCO amplitude suddenly becomes very large. At that time, U quickly decreases to 28.7 m/s although the rotational speed of the motor is not changed. This apparently is because the amplitude of the panel becomes large enough that the mean aerodynamic flow through the wind tunnel is changed.

Fig. 9 shows the responses of panel under the conditions of $U = 28.7$ m/s. This limit cycle oscillation is called a 'large amplitude LCO.'

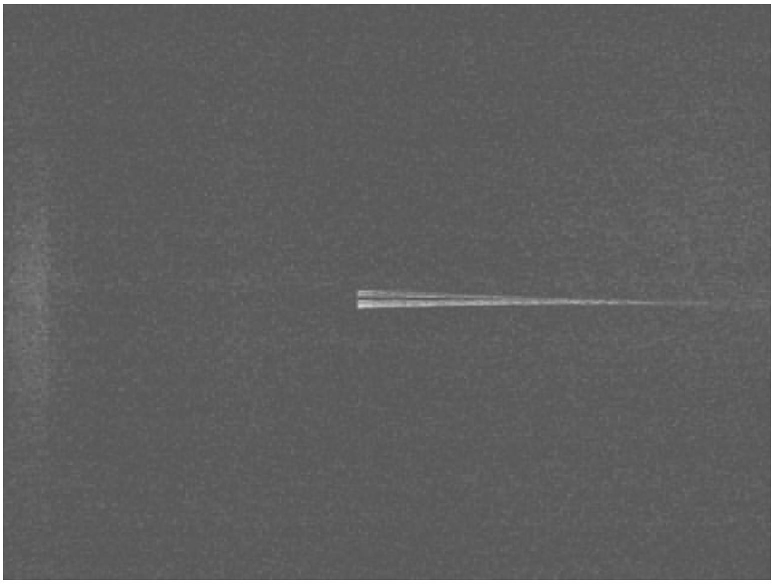

Fig. 6. Vibration mode of small-amplitude LCO ($U = 29.1$ m/s).

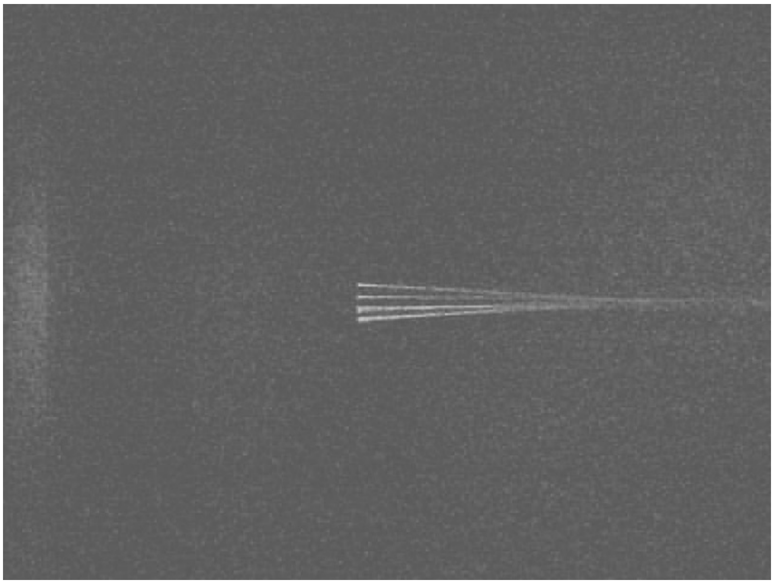

Fig. 7. Vibration mode of small-amplitude LCO ($U = 29.8$ m/s) (close-up view emphasizing the trailing edge portion of the flexible panel).

After large-amplitude LCO occurs, the rotational speed of the wind tunnel motor was increased and additional pictures taken of the panel. Fig. 10 show the response of the panel for $U = 29.8$ m/s. In this case, the amplitude becomes rather large. Now the rotational speed of the motor is decreased, i.e., U decreases, the pictures again are taken of the panel. Figs. 11 and 12 show the response of the panel for $U = 28.1$ and 27.5 m/s. From Figs. 10 to 12, it is seen that the amplitude decreases as U decreases. Finally, the large-amplitude LCO disappears when U falls below 27.3 m/s. At that time, U quickly increases to 27.8 m/s although the rotational speed of the motor has not changed.

Figure 13 shows the relationship between amplitude of the trailing edge of the panel and U. In this figure, the scenario is that U is increased until the large-amplitude LCO occurs and then the amplitude increases slightly as U increases further. However, once the large-amplitude LCO occurs, it does not disappear until U decreases

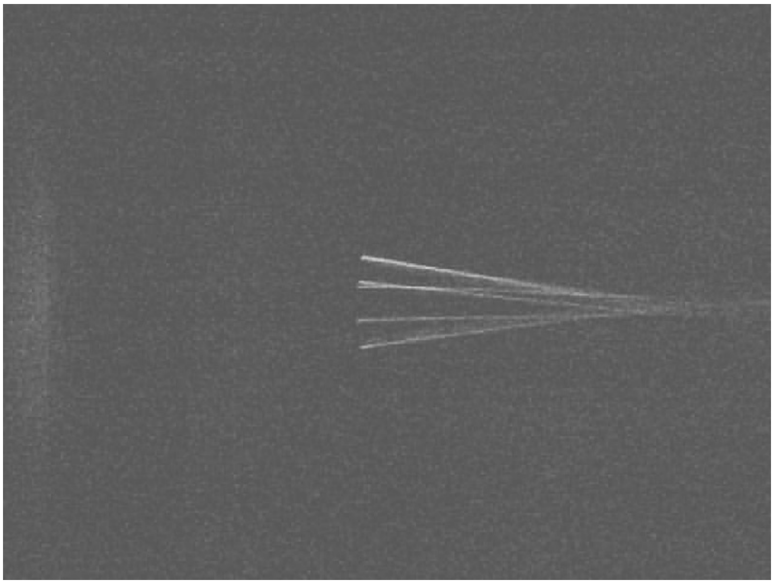

Fig. 8. Vibration mode of small-amplitude LCO ($U = 29.9\,\mathrm{m/s}$) (close-up view emphasizing the trailing edge portion of the flexible panel).

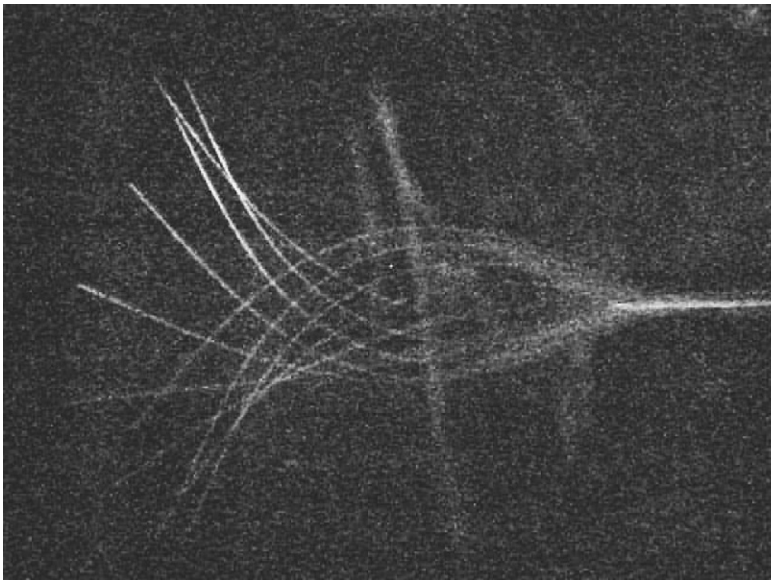

Fig. 9. Vibration mode of large-amplitude LCO ($U = 28.7\,\mathrm{m/s}$).

below 27.3 m/s. This hysteretic characteristic nonlinear response is a key feature of this phenomenon. The results for the response frequency are shown in Fig. 14.

Although the LCO behavior found experimentally is intriguingly complex, the results were repeatable.

4.2.2. *Theoretical results for LCO*

We have used a standard discrete time algorithm to calculate the nonlinear response of this aeroelastic system using the full aerodynamic model, Eq. (24), and also the reduced order aerodynamic model, Eq. (25). It is found that it is very

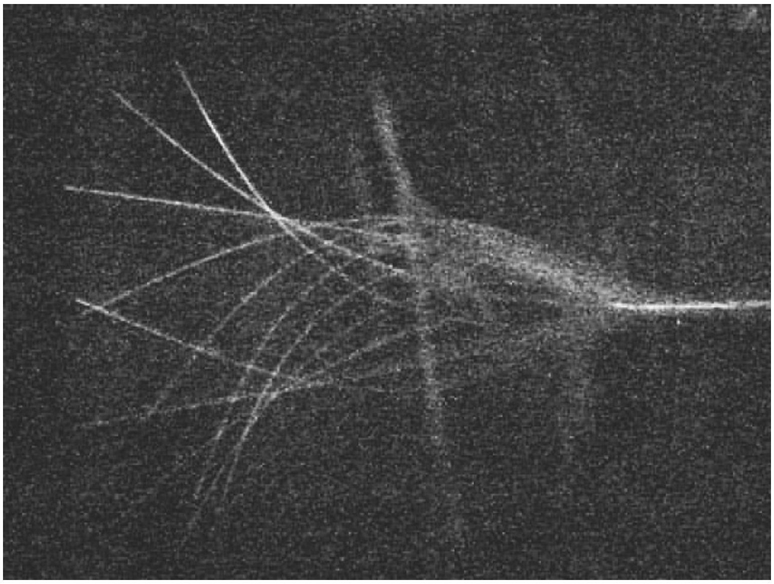

Fig. 10. Vibration mode of large-amplitude LCO ($U = 29.8\,\text{m/s}$).

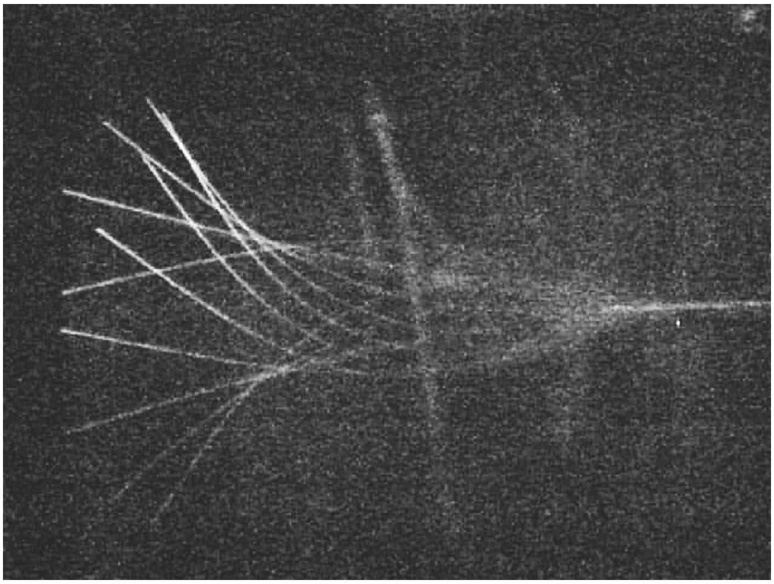

Fig. 11. Vibration mode of large-amplitude LCO ($U = 28.1\,\text{m/s}$).

costly to calculate the response using the full aerodynamic model because of long CPU times even when using a supercomputer, T916, in the North Carolina Supercomputing Center. Due to the mass or inertia nonlinearity, the mass matrix in Eq. (25) is not constant (independent of time) and thus one must invert this matrix at each time step. However, the reduced order aerodynamic model makes these calculations practical. Another benefit from the reduced order aerodynamic model is that we avoid a numerical divergence in the higher velocity range even when using a small dt. This is because the time step, dt, can be selected to be small enough to insure numerical stability whatever the dx of the original aerodynamic model (unlike the original vortex lattice model which requires changes in both dx and dt to maintain numerical stability).

A typical nondimensional transverse displacement time history and corresponding FFT analysis for $U = 30.0\,\text{m/s} > U_f = 29.5\,\text{m/s}$ are shown in Fig. 15(a,b) which uses the reduced order aerodynamic model with 11

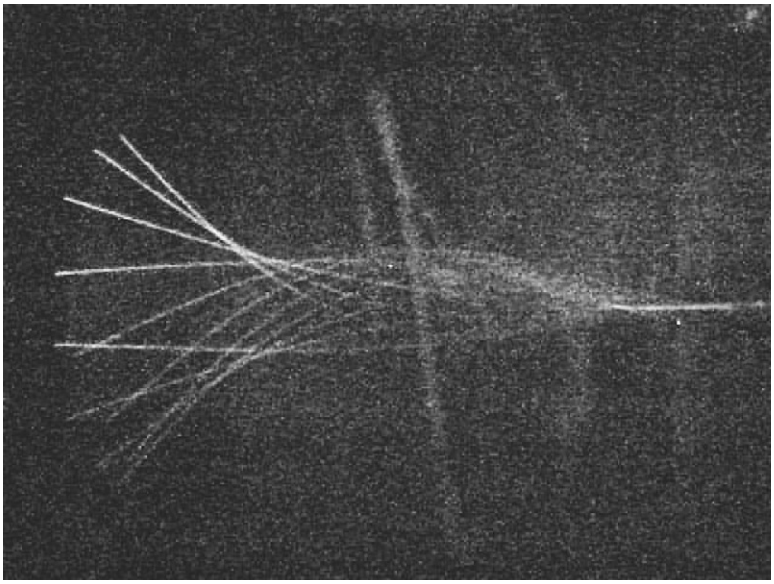

Fig. 12. Vibration mode of large-amplitude LCO ($U = 27.5\,\mathrm{m/s}$).

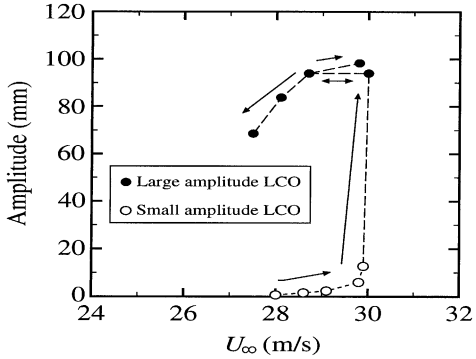

Fig. 13. LCO amplitude of panel trailing edge versus flow velocity.

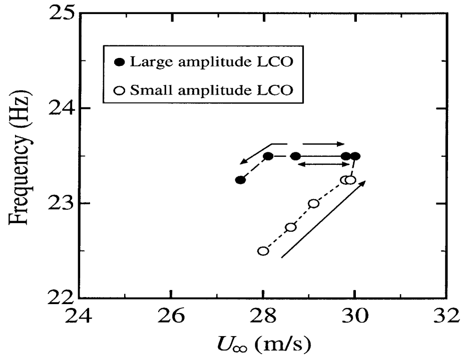

Fig. 14. LCO frequency versus flow velocity.

aerodynamic eigenmodes ($R_a = 11$). There is a steady-state limit cycle oscillation after a transient response of about 20 s. The dominant LCO frequency is $\omega = 22.25\,\mathrm{Hz}$ as shown in Fig. 15(b) by the solid line. Note that the LCO frequency is lower than the flutter frequency ($\omega_f = 22.5\,\mathrm{Hz}$) which is indicated by a dash–dot line. This is because the

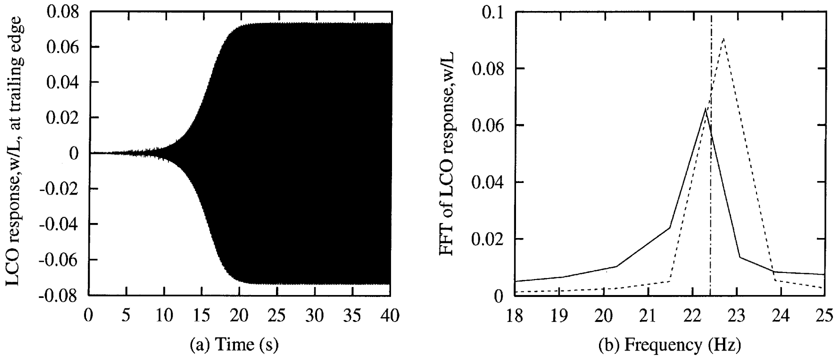

Fig. 15. LCO response for $U = 30\,\mathrm{m/s}$, (a) for time history and (b) for FFT analysis.

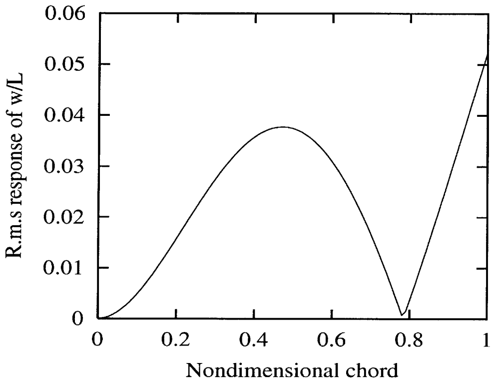

Fig. 16. R.m.s. of LCO vibration mode shape for $U = 30.0\,\mathrm{m/s}$.

effect of the nonlinear inertia terms on the LCO behavior is significant. This result is not surprising based upon the previous results for forced excitation. Recall Fig. 3(b). The nondimensional r.m.s. amplitude (w/L) is 0.052 at the trailing edge of the panel.

Corresponding to Fig. 15, the root mean square (r.m.s) of the LCO vibration mode shape for $U = 30.0\,\mathrm{m/s}$ is shown in Fig. 16. Recall Fig. 4(b) where it was found that the flutter mode is dominated by the second chordwise bending mode. The LCO mode shape is similar to the flutter mode with a node line near $x/L \approx 0.8^-$.

To consider effects of the number of structural modal functions included in the analysis, nx, on the limit cycle behavior and LCO frequency, additional LCO response calculations for $nx = 2$, 4 and 5 were made using the reduced order aerodynamic model with aerodynamic eigenmodes. The results are shown in Fig. 17(a,b) for the nondimensional peak amplitude, w/L, at the trailing edge of the elastic panel and also for the LCO frequency versus the number of modes. As the number of structural mode increases, the LCO amplitude decreases slightly for a given flow velocity. This is because the linear flutter velocity increases slightly when nx increases as shown in Fig. 5(a). When $nx \geqslant 3$, the LCO peak amplitude and frequency show good convergence.

To gain further insight into the LCO, the mass inertia nonlinear terms were removed and only the structural stiffness nonlinearity was retained, i.e., $\mathrm{d}M = F_M = 0$ in Eq. (25). The results are shown in Fig. 18. It is found that the system still has a steady-state limit cycle oscillation for the same flow velocity as in Fig. 15. The nondimensional r.m.s. amplitude (w/L) is now 0.065 at the trailing edge of the panel versus 0.052 when both stiffness and inertia nonlinearities are included. The FFT analysis of the steady-state LCO for this case is also shown in Fig. 15(b) as indicated by a broken line. The LCO frequency is 22.67 Hz and is slightly higher than the linear flutter frequency. It is evident that including only the structural stiffness nonlinearity leads to a higher LCO amplitude than when both mass and stiffness nonlinearities are included. Similar results were also observed from Fig. 3 for the forced excitation case. The mass inertia nonlinear terms not only provide an additional inertia force, but also an equivalent cubic spring force which render the LCO amplitude smaller.

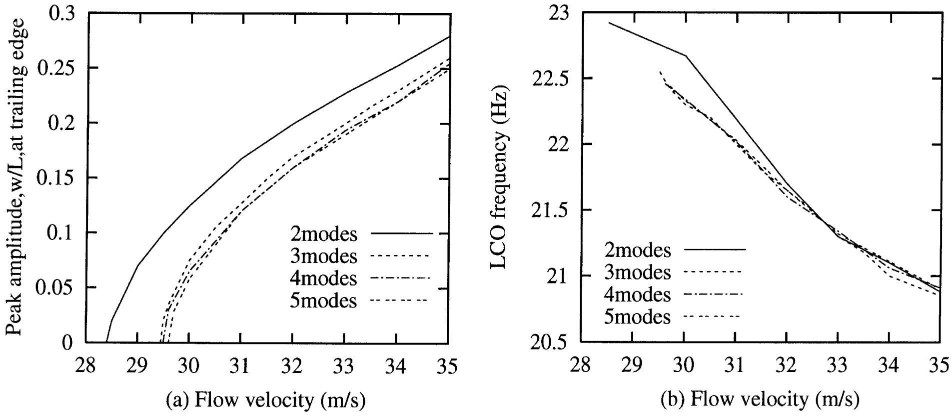

Fig. 17. LCO response versus flow velocity for different number of total structural modes, (a) for peak amplitude at trailing edge of the elastic panel and (b) for frequency.

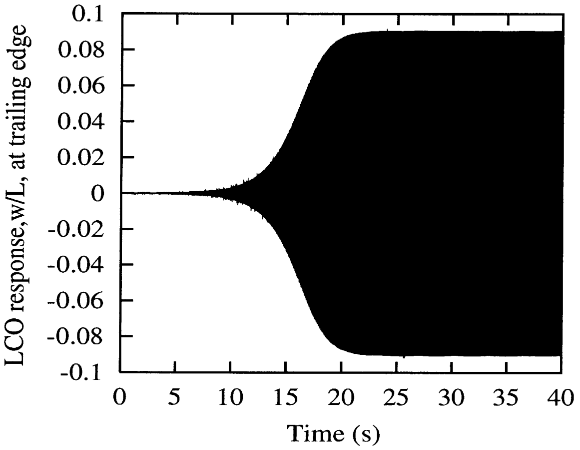

Fig. 18. Time history for $U = 30\,\text{m/s}$ and only stiffness nonlinearity is included.

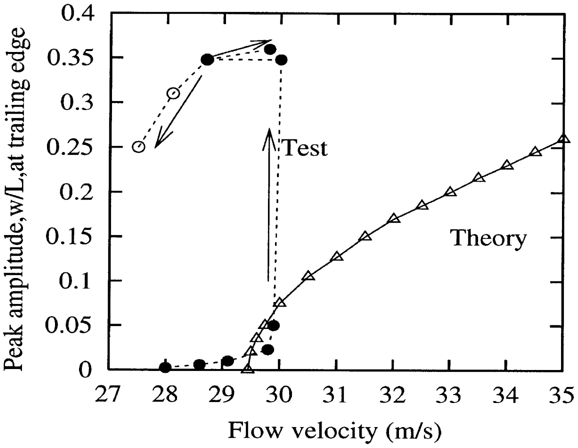

Fig. 19. Theoretical and experimental correlation of LCO nondimensional peak amplitude versus flow velocity.

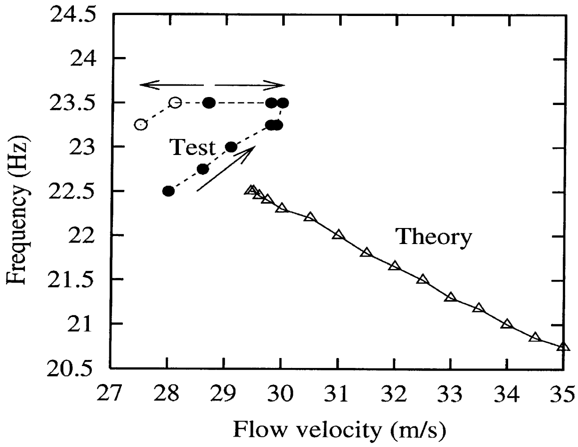

Fig. 20. Theoretical and experimental correlation of LCO frequency versus flow velocity.

When the flow velocity increases, the response has a higher amplitude with a dominant single oscillatory frequency and the oscillatory frequency decreases as shown in Figs. 19 and 20.

4.2.3. Theoretical and experimental correlation for flutter and LCO

Fig. 19 shows the theoretical and experimental nondimensional peak amplitude of the limit cycle oscillation versus the flow velocity. The theoretical results are obtained using the reduced order aerodynamic model with $R_a = 11$ and the number of structural modes is $nx = 3$. The experimental results are from Fig. 13 and normalized by the panel chord, L.

The flow velocity for the onset of flutter [and LCO] shows very good correlation between theory and experiment. However, the LCO responses per se show significant differences between predicted versus measured.

As seen in Fig. 19, as flow velocity increases the theoretical response amplitude increases, but there is no jump to be found at $U = 30\,\mathrm{m/s}$ as was seen in the experiment. Also we did not find any hysteretic phenomena in the theoretical calculations as was seen experimentally. The reason may be because the linear aerodynamic theory used here does not account for so large a structural motion on the aerodynamic forces. A nonlinear vortex lattice aerodynamic theory by Konstadinopoulos et al. (1985) and Mracek et al. (1992) could and perhaps should be considered in the present case. Clearly, the effects of structural nonlinearities alone are not sufficient to describe the experimental results for the large-amplitude LCO.

Also the change in the wind tunnel mean flow appears to be significant when the panel amplitude becomes large. A smaller experimental model (smaller L) or a larger wind tunnel would help reduce this effect. Pursuing either option presents some practical difficulties, but perhaps these can be overcome.

From a dimensional and order of magnitude analysis, aerodynamic nonlinearities should be negligible when the transverse deflection to panel chord ratio, w/L, is much less than one. See Dowell et al. (1995) and Dowell and Hall (2001). When the structural nonlinearities are sufficient to make w/L small enough (e.g. for the small-amplitude LCO as shown in Fig. 19) one may expect the aerodynamic nonlinearities to be unimportant. Of course, one cannot know a priori, whether w/L will be sufficiently small. Hence the present study.

Fig. 20 shows the theoretical and experimental LCO frequency versus the flow velocity. The experimental LCO frequency has a slight change with increasing or decreasing the flow velocity. The theoretical LCO frequency decreases as the flow velocity increases. This suggests the theoretical LCO response is dominated by the nonlinear inertial terms. Note the greatly expanded vertical scale in Fig. 20.

As shown in Fig. 16 (theory) and Fig. 10 (experiment), good agreement between theory and experiment for the LCO spatial shape is obtained, i.e., the LCO vibration spatial shape is dominated by the second chordwise bending mode as was the case at the onset of flutter.

To further investigate the above results, a FFT analysis at the root was made from typical theoretical and experimental strain histories. Fig. 21(a) shows the measured strain time history at the root (leading edge of the panel) and Fig. 21(b) shows the FFT analysis of theoretical and experimental results for $U = 30\,\mathrm{m/s}$ for the large-amplitude LCO. The theoretical LCO amplitude is substantially less than the measured values at this flow velocity as noted previously. These results are consistent with those obtained from the measured displacement responses using the photographic method for determining the response at the trailing edge of the panel.

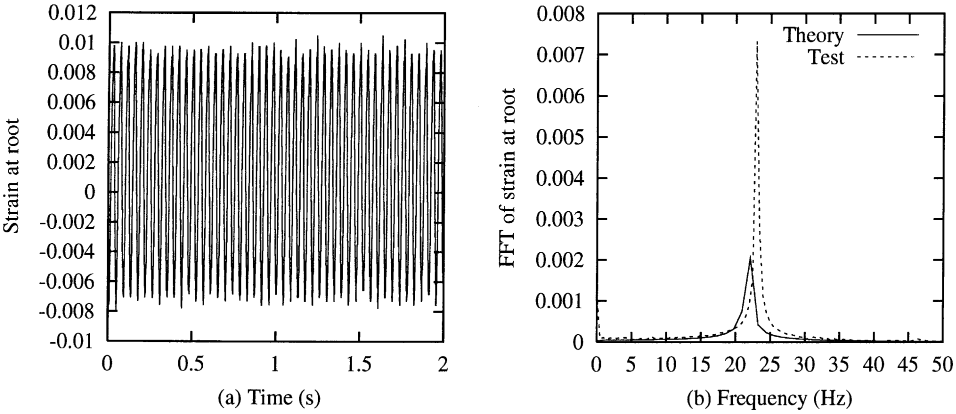

(a) Time (s)

(b) Frequency (Hz)

Fig. 21. LCO strain response at root for $U = 30\,\mathrm{m/s}$, (a) for measured time history and (b) for theoretical and experimental FFT analysis.

5. Concluding remarks

Nonlinear equations of motion for two-dimensional panels clamped at their leading edge in a three-dimensional low subsonic flow are derived by an energy method. Both nonlinear structural stiffness and inertia effects are included. A linear, three-dimensional aerodynamic model is used in the analysis.

This is the first work that has included a three-dimensional aerodynamic model for the flutter of a structure cantilevered at its leading edge in combination with a nonlinear structural model, i.e. that of Semler and Paidoussis (1994), for such a plate structure. Both theoretical and experimental results show that the flutter and LCO mode is dominated by the second panel bending mode. These results are qualitatively consistent with those of previous work by Kornecki et al. (1976), Huang (1995) and Shayo (1980) that used linear theory for both the structure and a two-dimensional aerodynamic flow.

Theory and experiment are in very good quantitative agreement as to the flow velocity at which flutter and LCO begins. By contrast, calculations using a more approximate aerodynamic theory, i.e., two-dimensional theory, are not in good quantitative agreement with the experiment for the onset of flutter.

A limit cycle oscillation is found when the flow velocity is increased beyond the linear flutter boundary. The theoretical LCO amplitude increases and LCO frequency decreases as the flow velocity increases. But the experimental LCO has a large jump in amplitude beyond a certain flow velocity and a LCO hysteretic phenomenon was also observed, neither of which are found in the present nonlinear structural, but linear aerodynamic theoretical model. The dynamic behavior of the LCO is found to be essentially a single harmonic oscillation, both theoretically and experimentally. For the present theoretical model, both the nonlinear structural stiffness and inertia contribute to LCO. However, the inertia nonlinearity is relatively more significant.

The significant differences observed between theory and experiment for the large LCO response are thought to be a result of aerodynamic nonlinearities not modelled in the present theory. A more refined model would include aerodynamic nonlinear effects. Here the work of Mook and colleagues (Konstadinopoulos et al., 1985; Mracek et al., 1992) could be used as a basis for such a model. Also, it is desirable to use a smaller test model or larger wind tunnel to decrease the change in the mean wind tunnel velocity flow due to the LCO, although either of these possibilities pose practical difficulties.

It is noted that even the smaller LCO amplitudes predicted by the present theory would appear to be unacceptable in many design applications, although there may still be some utility of this LCO for other applications, e.g. flow control.

The hope and indeed expectation has been that for some range of flow velocities beyond the onset of flutter the structural nonlinearities would be dominant and any aerodynamic nonlinearities could be neglected. It now appears that the range of flow velocities for which the aerodynamic nonlinearities can be neglected is quite small, though the authors believe discernible. Thus clearly if the LCO is to be modelled theoretically for a significant range of velocities beyond the onset of flutter and LCO, aerodynamic nonlinearities must be included. This is a sobering conclusion because the modelling of the aerodynamic nonlinearities is a far greater challenge than modelling the structural nonlinearities. Of course, including the structural nonlinearities with a three-dimensional linear aerodynamic model represents a significant step forward from previous analysis. However, another large step remains to be taken if the large-amplitude LCO observed experimentally is to be modelled theoretically using a nonlinear aerodynamic model.

Acknowledgements

This work was supported by AFOSR Grant "Dynamics and Control of Nonlinear Fluid–Structure Interaction" under the direction of Dr. Dan Segalman. All numerical calculations were done on a supercomputer, T916, in the North Carolina Supercomputing Center (NCSC).

References

Doggett, R.V., Solstmann, D.L., 1989. Some low-speed flutter characteristics of simple low-aspect-ratio delta wing models. NASA TM 101547.

Dowell, E.H., Crawley, E.F., Curtiss Jr., H.C., Peters, D.A., Scanlan, R.H., Sisto, F., 1995. A modern Course in Aeroelasticity, 3rd Edition. Kluwer Academic Publishers, Dordrecht.

Dowell, E.H., Hall, K.C., 2001. Modelling of fluid–structure interaction. Annual Review of Fluid Mechanics 33, 445–490.

Huang, L., 1995. Flutter of cantilevered plates in axial flow. Journal of Fluids and Structures 9, 127–147.

Joseph, K., Allen, P., 1991. Low-Speed Aerodynamics, McGraw-Hill, Inc. New York, p. 297.

Konstadinopoulos, A., Thrasher, D.F., Mook, D.T., Nayfeh, A.H., Watson, L., 1985. A vortex-lattice method for general unsteady aerodynamics. Journal of Aircraft 22, 43–49.

Kornecki, A., Dowell, E.H., O'Brien, J., 1976. On the aeroelastic instability of two-dimensional panels in uniform incompressible flow. Journal of Sound and Vibration 47, 163–178.

Mracek, C.P., Kim, K.L., Mook, D.T., 1992. Three-dimensional potential flows by a vorticity-panel method. Computers and Fluids 21, 31–42.

Paidoussis, M.P., 1998. Fluid–Structure Interactions. . Slender Structures in Axial Flow, Vol. 1. Academic Press, London.

Semler, C., Paidoussis, M.P., 1994. The nonlinear equations of motion of pipes conveying fluid. Journal of Sound and Vibration 169, 577–599.

Shayo, L.K., 1980. Stability of cantilever panels in uniform incompressible flow. Journal of Sound and Vibration 68, 341–350.

Taneda, S., 1968. Waving motions of flag. Journal of the Physical Society of Japan 24, 392–401.

Tang, D.M., Herry, J.K., Dowell, E.H., 1999. Limit cycle oscillations of delta wing models in low subsonic flow. AIAA Journal 37, 1355–1362.

Tang, D.M., Dowell, E.H., 2001a. Effects of angle of attack on nonlinear flutter of a delta wing. AIAA Journal 39, 15–21.

Tang, D.M., Dowell, E.H., 2001b. Limit cycle oscillations of two-dimensional panels in low subsonic flow. International Journal of Nonlinear Mechanics 37, 1199–1209.

Yadykin, Y., Tenetov, V., Levin, D., 2000. The drag of a flexible strip hanging vertically in a parallel flow. AIAA Paper 2000-4228.